UC Berkeley
UC Berkeley Previously Published Works

Title

In Situ ATR–SEIRAS of Carbon Dioxide Reduction at a Plasmonic Silver Cathode

Permalink

Journal

ISSN

Authors

Corson, Elizabeth R
Kas, Recep
Kostecki, Robert
et al.

Publication Date

DOI

Supplemental Material

Peer reviewed

In Situ ATR-SEIRAS of Carbon Dioxide Reduction at a Plasmonic Silver Cathode

Elizabeth R. Corson,[†,‡] Robert Kostecki,[†,¶] Jeffrey J. Urban,[†,§] Bryan D. McCloskey,[*,†,‡,¶] and Ruud Kortlever[*,‖]

†*Joint Center for Artificial Photosynthesis, Lawrence Berkeley National Laboratory, Berkeley, California 94720, USA*

‡*Department of Chemical and Biomolecular Engineering, University of California, Berkeley, California 94720, USA*

¶*Energy Storage and Distributed Resources Division, Lawrence Berkeley National Laboratory, Berkeley, California 94720, USA*

§*The Molecular Foundry, Lawrence Berkeley National Laboratory, Berkeley, California 94720, USA*

‖*Department of Process & Energy, Faculty of Mechanical, Maritime & Materials Engineering, Delft University of Technology, 2628 CB Delft, The Netherlands*

Abstract

Illumination of a voltage-biased plasmonic Ag cathode during CO_2 reduction results in a suppression of the H_2 evolution reaction while enhancing CO_2 reduction. This effect has been shown to be photonic rather than thermal, but the exact plasmonic mechanism is unknown. Here, we conduct an in situ ATR-SEIRAS study of a sputtered thin film Ag cathode on a Ge ATR crystal in CO_2-saturated 0.1 M $KHCO_3$ over a range of potentials

1

in both dark and illuminated (365 nm, 125 mW cm^{-2}) conditions to elucidate the nature of this plasmonic enhancement. We find that the onset potential of CO_2 reduction to adsorbed CO on the Ag surface is -0.25 V_{RHE} and is identical in the light and the dark. As the production of gaseous CO is detected in the light near this onset potential but is not observed in the dark until -0.5 V_{RHE} we conclude that the light must be assisting the desorption of CO from the surface. Furthermore, the HCO_3^- wavenumber and peak area increase immediately upon illumination, precluding a thermal effect. We propose that the enhanced local electric field that results from the LSPR is strengthening the HCO_3^- bond, further increasing the local pH. This would account for the decrease of H_2 formation and increase of CO_2 reduction products in the light.

Introduction

Electrochemical carbon dioxide (CO_2) reduction creates chemicals and fuels from electricity, water, and CO_2 that would have otherwise been released to the atmosphere. By using renewable electricity the process can be carbon-neutral, replacing thermochemical methods that consume fossil fuels. To be cost-competitive we need CO_2 electrocatalysts that can operate at low overpotentials and have high selectivity.[1] We have approached this challenge through plasmon-enhanced electrochemical conversion (PEEC).

PEEC is the application of potential to a plasmonically active electrode while illuminating the surface to impact the electrocatalytic performance. PEEC has been shown to impact the product distribution and decrease overpotentials for CO_2 reduction,[2,3] oxygen (O_2) reduction,[4,5] and hydrogen (H_2) evolution[6–8]. While these effects have been shown to be photonic in nature, it is difficult to pinpoint the exact plasmonic mechanism.

In this study, we use in situ ATR-SEIRAS (attenuated total reflectance surface enhanced infrared absorption spectroscopy) to understand how the electric double layer (EDL) structure

changes with applied potential, time, and illumination and how this impacts CO_2 reduction at a plasmonic Ag cathode. In previous work we demonstrated that a plasmonic Ag cathode showed significant differences in the product distribution and overpotential during CO_2 reduction in the dark and under 365 nm LED illumination, which was near the plasmon resonance peak for the Ag electrode (351 nm).[3] At low overpotentials carbon monoxide (CO) production was enhanced and H_2 evolution was suppressed upon illumination. In addition, the onset potential for CO production appeared to be reduced by 300 mV in the light compared to the dark. Formate production was enhanced in the light at potentials more cathodic than -0.7 V_{RHE} and methanol was only formed under illuminated conditions at potentials more cathodic than -0.8 V_{RHE}, reaching a maximum Faradaic efficiency (FE) of nearly 2% at -1.1 V_{RHE}.[3] This represents a 550 mV decrease in the overpotential and a 100-fold increase in selectivity for methanol production when compared to CO_2 reduction on a polycrystalline Ag foil in the dark.[9]

Studies have been published on infrared (IR) spectroscopy during electrochemical CO_2 reduction in aqueous electrolytes on cathodes such as Ag,[10,11] Au,[12] and Cu[10,13–15] with a review of recent work presented by Kas et al.,[16] although none have explored PEEC combined with in situ IR spectroscopy measurements. In fact, only a handful of studies have used IR spectroscopy to study photocatalytic reactions at illuminated catalysts, including aqueous photoreduction of O_2,[17] photooxidation of water,[18,19] and photooxidation of glyoxylic acid.[20] Here, we use ATR-SEIRAS to provide new insights into the potential-dependent structure of the EDL at a negatively-biased Ag cathode in an aqueous electrolyte and present further clues into the possible mechanism of plasmon-enhanced electrochemical CO_2 reduction.

Experimental Methods

Cathode Fabrication

To prepare the cathode, a 60° Ge ATR crystal (Pike Technologies, 013-3132) was polished three times with subsequently smaller diameter alumina suspensions of 1.0 μm, 0.3 μm, and 0.05 μm (Buehler, 40-10081, 40-10082, and 40-10083) using microcloth pads (BASi, MF-1040). The crystal surface was cleaned with water and acetone using lint-free wipes and dried with compressed nitrogen. The crystal was placed in a Faraday cage and subjected to air plasma for 8 minutes on high power (Harrick Plasma, PDC-002-CE). A 40 nm film of Ag was deposited on the crystal surface in a custom-built sputtering tool with an argon (Ar) pressure of 50 μbar, deposition rate of 0.01455 nm s^{-1}, and substrate rotation of 15° s^{-1}. After deposition, the resistance across the surface of the cathode was typically 4–8 Ω, as measured by a multimeter. A schematic of the cathode is shown in Figure S2.

Cathode Surface Imaging and Profiling

Scanning electron microscopy (SEM) images were taken with a Thermo Scientific Quanta FEG 250 SEM. Atomic force microscopy (AFM) measurements were performed with a commercial AFM system (Bruker Dimension Icon) using the PeakForce Quantitative Nanoscale Mechanical tapping mode under ambient conditions. X-ray photoelectron spectroscopy (XPS) measurements were acquired with a Thermo Scientific K-Alpha XPS.

In Situ ATR-SEIRAS Measurements

SEIRAS experiments were performed in a custom, single chamber electrochemical cell (Figure S1).[16] A 0.05 M solution of potassium carbonate (K_2CO_3) (Alfa Aesar, 10838, 99.997%

metals basis) was prepared with 18.2 MΩ deionized water from a Millipore system, which became 0.1 M potassium bicarbonate ($KHCO_3$) when saturated with CO_2. The anode was a graphite rod (Alfa Aesar, 40766, 99.9995% metals basis) and the reference electrode was Ag/AgCl with 3 M NaCl (BASI, MF-2052). All potentials were converted to and reported versus the reversible hydrogen electrode (RHE). All electrochemical measurements were IR-corrected and performed with a Biologic SP-200 potentiostat. CO_2 flowed through the electrolyte for 30 minutes before the start of an experiment, and continued flowing throughout the experiment. Additionally, the ATR attachment and the chamber surrounding it were purged with nitrogen (N_2) for 30 minutes before the start of an experiment. Before use, the cathode surface was activated by three cyclic voltammetry (CV) scans at 50 mV s^{-1} (Figure S3) from -0.50 to approximately 0.70 V_{RHE}. The anodic potential was adjusted to keep the current density below 0.80 mA cm^{-2} to prevent film degradation.

SEIRAS spectra reported during CV were an average of 32 spectra taken at a resolution of 8 cm^{-1}. A new background spectrum (Figure S10) was taken for each experiment during chronoamperometry (CA) at 0.2 V_{RHE} before continuing to the CV from 0.2 to -0.9 V_{RHE} at 2 mV s^{-1}. The negative logarithm of the ratio between the single beam sample spectrum (R) and the single beam background spectrum (R_0) gives the absorbance (A) spectrum of the sample in absorbance units (a.u.): $A = -\log(R/R_0)$. The return scan continued to potentials more anodic than 0.2 V_{RHE} and was stopped when the SEIRAS spectrum was as close to the baseline as possible. See Figure S11 for representative SEIRAS spectra from 0.2 to 0.6 V_{RHE}.

SEIRAS spectra reported during CA were an average of 32 spectra taken at a resolution of 8 cm^{-1} or, if designated as "high-resolution", an average of 72 spectra taken at a resolution of 4 cm^{-1}. A new background spectrum was taken for each experiment during CA at 0.2 V_{RHE} before continuing to the applied potential of the CA experiment. After 90 seconds of CA a linear voltammetry sweep (LSV) was performed at 5 mV s^{-1} to an anodic potential

where the SEIRAS spectrum was as close to the baseline as possible.

Photoelectrochemical Measurements

The electrode was illuminated through the center port of the cell using a Mightex Systems LCS-0365-48-22 365 nm ultrahigh-power LED. During illuminated SEIRAS experiments the light intensity at the surface of the cathode was 125 mW cm^{-2}. During illuminated product analysis experiments the light intensity at the surface of the cathode was 170 mW cm^{-2}. The incident power was measured with a Coherent PowerMax PM10 power meter connected to a Coherent LabMax-TOP power meter console.

Product Measurements

Experiments for product analysis were performed in a custom cell described by Corson et al.[21] Gaseous products were analyzed by an in-line Multiple Gas Analyzer #5 SRI Instruments GC with a 12 ft HayeSep D (divinylbenzene) column, thermal conductivity detector (TCD), flame ionization detector (FID) preceded by a methanizer, and Ar carrier gas. For a single product analysis run, a constant potential was applied for 16 minutes with GC injections at 3 and 15 minutes. The results from the 15 minute injection are reported here. Gaseous product concentrations were calculated from a calibration curve of at least three different concentrations for each gas type. Liquid products in the catholyte and anolyte were quantified after the electrolysis was complete by ^{1}H NMR spectroscopy on a Bruker Avance III 500 MHz magnet. Liquid product concentrations were determined by using phenol and DMSO as internal standards.[22] Complete details on the GC and NMR calibration and quantification methods are reported in Corson et al.[21]

Results and Discussion

Cathode Fabrication

The cathode fabrication method was optimized to synthesize a Ag thin film that both enhanced the SEIRAS signal while remaining stable and intact during (photo)electrochemical experiments. Preparation of Ag films for ATR-SEIRAS using vacuum evaporation, chemical deposition, and Ar sputtering have previously been reported.[23,24] Our cathode fabrication method was guided by prior studies that showed how sputtered Ag thin film morphology was influenced by changes in the deposition rate, sputtering pressure, substrate temperature, sputtering gas, and film thickness.[24–26]

Sputtering thin films of Ag at 3 μbar of Ar pressure on bare Ge or Si ATR crystals resulted in films with limited SEIRAS signal that delaminated quickly. A thin (0.5–3 nm) Ti adhesion layer deposited on the Ge or Si crystal before depositing the Ag layer produced extremely stable cathodes, however these displayed no SEIRAS signal. To improve adhesion via an alternate route, the crystal was cleaned with air plasma before deposition. To enhance the SEIRAS signal, the sputtering pressure was increased to 50 μbar which decreases the mean-free path length of the sputtered atoms. This results in collisions and agglomeration of the Ag atoms before deposition, producing a rougher surface.[25] This technique created a Ag film on a Ge crystal that was both stable and SEIRAS-active, but the Ag film on a Si crystal remained unstable.

However, the SEIRAS activity of the Ag film on a Ge crystal was still not sufficient. Figure S4 shows an example of SEIRAS spectra collected during a CV scan on an as-deposited Ag cathode prepared using the optimized deposition method. Spectroscopic peaks are observed, but they are small and deformed. To further enhance the SEIRAS signal, the surface was activated by three CV scans. A representative CV curve is shown in Figure S3. SEM and

AFM images (Figure S5 and Figure S6) before and after activation show that the surface is further roughened by this CV cycling. Larger grains (75–150 nm) are formed on the surface and the grain size distribution of the Ag film increases after activation, expanding the population of both small and large features. AFM root mean square (RMS) roughness increases from 3.7 nm on the as-deposited film to 5.6 nm on the activated film.

XPS measurements taken on the as-deposited cathode (after sputtering) show Ag to be the predominant component (Figure S7). There are small peaks for Ge and the environmental contaminants of O and C. Extremely small Cu peaks were resolved only by focusing on the region for Cu $2p_{1/2}$ and Cu $2p_{3/2}$ and increasing the acquisition time. XPS measurements of the same cathode after activation by CV cycling show an increase in the Ge peaks and a reduction of the Cu peaks to a signal that is barely distinguishable from the noise. The source of this trace Cu contamination is believed to be from the sputtering chamber. Complete removal of the Cu was verified by gaseous and liquid product analysis at -0.60, -0.75, and -0.80 V_{RHE} of Ag cathodes sputtered under the same conditions on glass slides with a 3 nm Ti adhesion layer. The FE and partial current densities shown in Figure S8 and Figure S9 for H_2, CO, and formate under dark and illuminated conditions closely match the results we reported for an e-beam deposited Ag cathode.[3] If any Cu were present we would expect to detect methane, ethylene, and ethanol in this potential range.[22] Any Ge on the surface is not expected to influence the SEIRAS results as Ge is not an active catalyst for CO_2 reduction, a bare Ge crystal showed no peaks during a CV scan in otherwise identical electrochemical conditions, and it has been shown that CO does not adsorb to a Ge ATR crystal.[27]

SEIRAS spectra from an activated Ag cathode (Figure 1) show multiple distinct peaks. The SEIRAS signal could be further enhanced by more aggressive CV cycling, but the film stability would be greatly diminished. The activation method described above resulted in a Ag film that could withstand hours of successive (photo)electrochemical experiments at modest applied potentials. CV scans could be performed up to -0.9 V_{RHE} and CA experiments could

be run up to -0.7 V_{RHE} without film delamination. The cathode was visually inspected after each experiment to confirm that the film was intact. A new cathode was prepared each day.
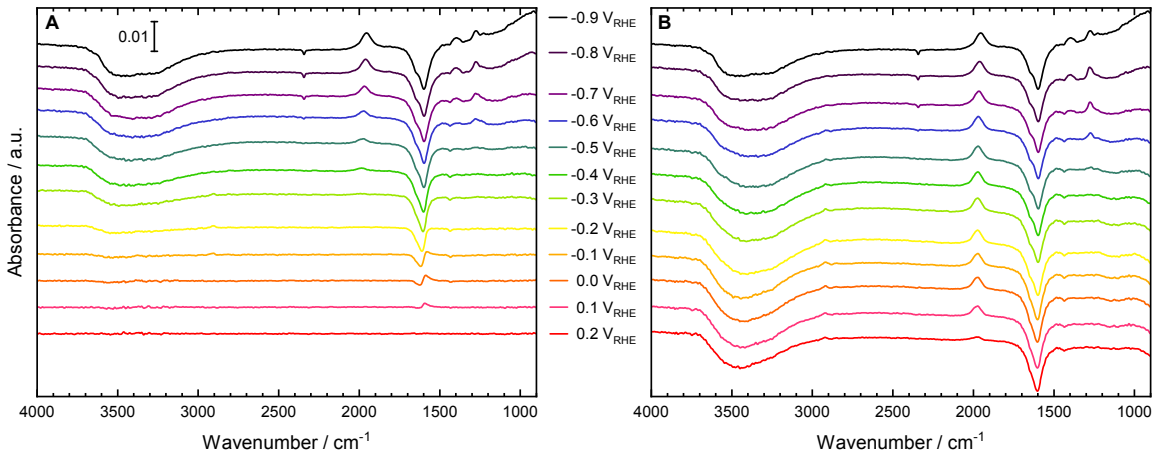
Peak Assignment

Figure 1: SEIRAS spectra taken during a CV scan at 2 mV s^{-1}. (A) shows the cathodic scan from 0.2 to -0.9 V_{RHE} and (B) shows the anodic scan from -0.9 to 0.2 V_{RHE}. The activated Ag cathode on a Ge ATR crystal was in a 0.1 M KHCO$_3$ electrolyte with a continuous CO$_2$ purge through the electrolyte. The background spectrum was taken at 0.2 V_{RHE}. The scale bar in (A) gives the y-axis scale in absorbance units (a.u.) and applies to both (A) and (B). The peaks are HCO$_3^-$ (1278 cm^{-2}), CO$_3^{2-}$ (1395 cm^{-2}), δ^{HOH} (1600 cm^{-2}), CO (1970 cm^{-2}), CO$_2$ (2342 cm^{-2}), and ν^{OH} (3402 cm^{-2}).

In Figure 1A the system is first held at 0.2 V_{RHE}, close to the open circuit voltage (OCV), to measure the background spectrum (Figure S10). At OCV we expect that there are no CO$_2$ reduction products adsorbed on the Ag surface, as no CO$_2$ reduction has occurred. As the OCV is approximately 300 mV above the point of zero charge (pzc) for Ag, we expect the surface to have a slightly positive charge that will influence the orientation of the water molecules.[28,29] The concentration of components in the bulk electrolyte is [H$_2$O] $\gg$ [K$^+$] > [HCO$_3^-$] > [CO$_2$] > [CO$_3^{2-}$] > [H$^+$] > [OH$^-$]. The concentration of components in the EDL at OCV is expected to be similar to that of the bulk, but with a somewhat higher representation of negatively charged species due to the slightly positive surface charge of the electrode. The potential is scanned cathodically at 2 mV s^{-1} to -0.9 V_{RHE} with a

new SEIRAS spectrum taken every 10 seconds. Peaks that appear in the spectra represent changes in the concentration or orientation of surface and near-surface species with respect to the OCV baseline. "Near-surface" species are those in the 5–10 nm region that can be detected by ATR-SEIRAS, with stronger signals coming from molecules closest to the surface due to the strength of the evanescent IR wave.[12] Water peaks signify changes in the orientation of water molecules, which will be discussed more extensively in the Water Bend and Stretch section.[28,30] Positive peaks corresponding to other species represent an increase in concentration at or near the surface, and negative peaks indicate a decrease in concentration at or near the surface.

At 0.1 V_{RHE} a peak appears at 1597–1623 cm^{-1} that is attributed to the HOH bend vibration (δ^{HOH}).[10,11,30,31] From 0.1 to -0.1 V_{RHE} the δ^{HOH} feature comprises a positive and negative component, with the positive part disappearing at -0.2 V_{RHE}. At this same time a broad, negative peak is observed at 3351–3520 cm^{-1} that is assigned to the O-H stretch absorption (ν^{OH}).[10,29–31] By -0.4 V_{RHE} we observe a single positive peak at 1962–1981 cm^{-1} which is attributed to CO that has formed from the reduction of CO_2 and is adsorbed on the surface.[10,32] Finally, by -0.7 V_{RHE} we see the three remaining peaks observed in this study: a positive HCO_3^- peak at 1276–1279 cm^{-1}, a positive CO_3^{2-} peak at 1393–1401 cm^{-1}, and a negative CO_2 peak at 2342 cm^{-1}.[11,12,31] The average position of each peak and the corresponding standard deviation is listed in Table 1; they are calculated from five CV scans performed during different experiments with newly prepared cathodes.

The anodic scan from -0.9 to 0.2 V_{RHE} is shown in Figure 1B. The peaks for HCO_3^-, CO_3^{2-}, and CO_2 disappear near the same potential of their appearance. The remaining peaks, however, display extreme hysteresis in the anodic scan; the peaks for CO, δ^{HOH}, and ν^{OH} still remain at 0.2 V_{RHE}. The average values of the potential when each peak appears and disappears are shown in Figure 2 along with the cyclic voltammogram corresponding to Figure 1. The tabulated values and standard deviations are shown in Table S1.

Table 1: Average SEIRAS peak positions[a]

Peak	Average Position (cm^{-1})
Bicarbonate (HCO_3^-)	1278 ± 1.9
Carbonate (CO_3^{2-})	1395 ± 3.8
Water Bend (δ^{HOH})	1600 ± 1.1
CO	1970 ± 2.7
CO_2	2342 ± 0.0
Water Stretch (ν^{OH})	3402 ± 22.6

[a] Average values and standard deviations are calculated from five CV experiments performed on different days with a new cathode prepared each day.

We will discuss what these trends imply for the behavior of each species in the following sections, but it is apparent that scanning the potential back to the OCV is not sufficient for returning the cathode surface and the EDL to their initial states. If, after an electrochemical experiment, the system is simply returned to OCV before beginning the next experiment, the SEIRAS peak trends may appear to be quite different. This is a result of the adsorbates formed during the previous experiment remaining on the surface and the different EDL structure. In this study the surface was "reset" back to the initial conditions after every experiment by continuing to scan to more anodic potentials. Figure S11 shows the SEIRAS spectra from 0.2 to 0.6 V_{RHE}. Adsorbed CO is completely removed from the surface by 0.3 V_{RHE} and the δ^{HOH} and ν^{OH} peaks cross the baseline and become positive around 0.4 V_{RHE}. The δ^{HOH} peak goes from a negative peak, to overlapping positive and negative peaks, to a positive peak during this anodic scan, similar to the behavior observed at the beginning of the cathodic scan from 0.1 to -0.1 V_{RHE}. As these two water-related peaks flip from positive to negative at different potentials, there is no potential where the original baseline is achieved. For every experiment presented in this study the anodic scan was stopped when the SEIRAS spectrum was as close to the baseline as possible.

The cathode surface can also be reset by letting the system equilibrate at OCV. Figure S14 shows the SEIRAS spectra during 30 minutes of OCV and Figure 4 shows the corresponding
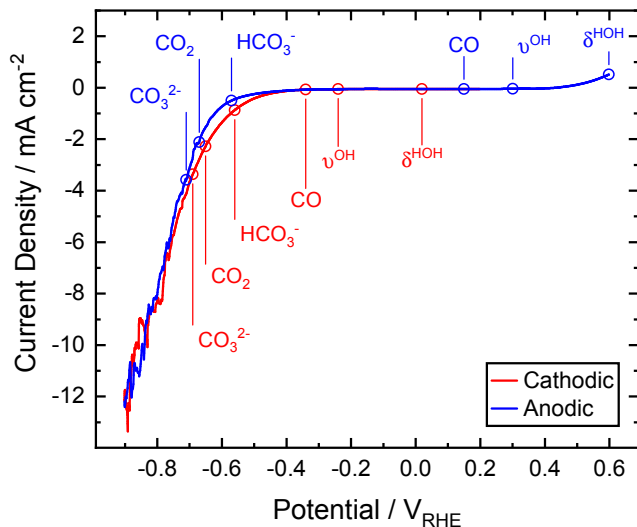
Figure 2: Cyclic voltammogram (CV) of a Ag cathode in a 0.1 M KHCO3 electrolyte recorded at a scan rate of 2 mV s^{-1} corresponding to the spectra displayed in Figure 1. The average potential of the appearance of each SEIRAS peak is marked (red circles) as the potential is scanned from 0.2 V$_{RHE}$ to -0.9 V$_{RHE}$ (cathodic scan). The average potential of the disappearance of each SEIRAS peak is marked (blue circles) as the potential is scanned from -0.9 V$_{RHE}$ to 0.6 V$_{RHE}$ (anodic scan). Average values are calculated from five CV experiments performed on different days with a new cathode prepared each day.

normalized peak areas. While CO desorbs from the surface after 10 minutes, the δ^{HOH} and ν^{OH} peaks continue to change. Eventually, these peaks will become positive and reach a steady state that is distinct from the initial baseline recorded under OCV conditions, but it could take as long as two hours in this particular electrochemical cell with a continuous purge of CO_2 through the electrolyte for convection. The time for stabilization during OCV is likely highly dependent on the geometry of the cell and the degree of electrolyte mixing. That the final steady-state EDL structure is different from the initial conditions may reflect subtle changes in the cathode surface resulting from the electrochemical experiment.

In the next sections we will discuss the significance of the trends presented here, as well as the differences observed during measurements in the dark and in the light. A more detailed analysis of the trends during cathodic and anodic CV scans are shown in Figure 3 where the average peak positions and normalized areas for the CO, δ^{HOH}, and ν^{OH} peaks are plotted. Similar plots for HCO_3^-, CO_3^{2-}, and CO_2 peaks are shown in Figure S12.
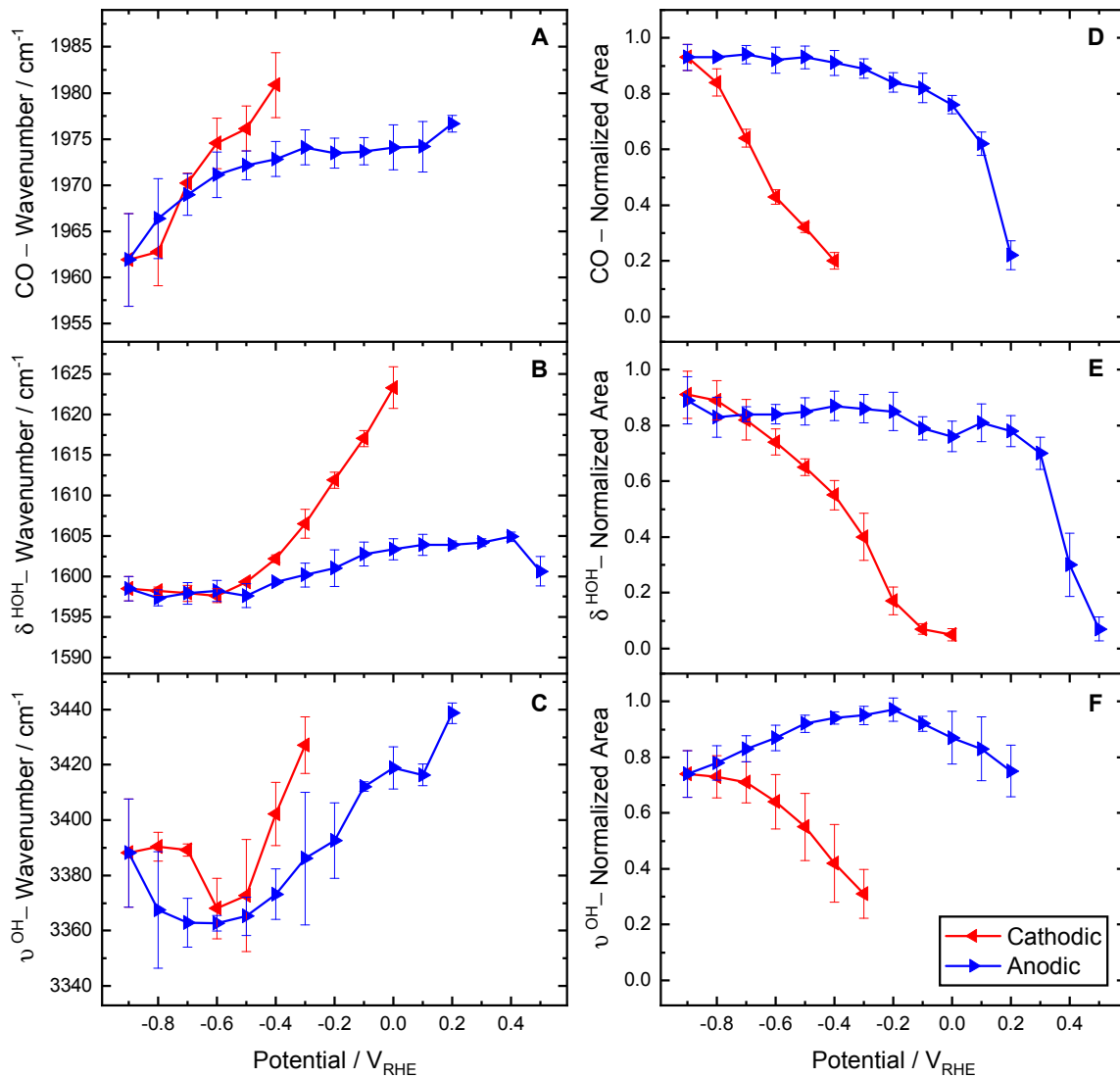
Figure 3: Average position (A–C) and normalized area (D–F) of three SEIRAS peaks during CV: CO (A and D), δ^{HOH} (B and E), and ν^{OH} (C and F). Average values and standard deviations are calculated from five CV experiments performed at 2 mV s^{-1} on different days with a new cathode prepared each day. The area is normalized by the largest area in each individual data set. Error bars represent one standard deviation. Red lines show the cathodic scan from 0.2 to -0.9 V$_{RHE}$ and blue lines show the anodic scan from -0.9 to 0.6 V$_{RHE}$. The activated Ag cathode on a Ge ATR crystal was in 0.1 M KHCO$_3$ with continuous CO$_2$ flow through the electrolyte.

Carbon Monoxide

In this study the CO signal appears as a single positive peak whose position ranges from 1962–1981 cm^{-1} with an average value of 1970 cm^{-1} (Table 1). This position and peak

shape matches closely with other reports of CO adsorbed linearly on Ag in electrochemical conditions: 1990 cm^{-1} in 0.1 M NaClO$_4$ at -0.15 V$_{RHE}$[32] on polycrystalline Ag and 1980 cm^{-1} in 0.05 M Na$_2$SO$_4$ at -0.2 V$_{RHE}$ for seven monolayers of Ag over platinum (Pt).[10] In contrast, two peaks for linearly adsorbed CO are reported for Cu electrodes: 1983 and 2103 cm^{-1} in 0.05 M Na$_2$SO$_4$ at -0.2 V$_{RHE}$ for six monolayers of Cu over Pt[10] and 2050 and 2080 cm^{-1} in 0.1 M KHCO$_3$ at -0.4 V$_{RHE}$ at a Cu thin film.[14] The fact that we observe a single CO peak at a much lower wavenumber provides further evidence that no Cu is present on the cathode surface, corroborating our XPS (Figure S7) and product analysis (Figure S8 and Figure S9) results. Furthermore, bridged CO, where the C is bonded to two metal atoms, is commonly reported on Pt surfaces in the 1750–1850 cm^{-1} range[31,33,34] but has not been reported for Ag surfaces. We do not observe any peaks at 1750–1850 cm^{-1}, providing further confirmation of a Ag surface that is not contaminated with other metals.[35]

The CO peak experiences a shift in position from 1981 to 1962 cm^{-1} on the cathodic scan that is largely reversible on the anodic scan, only deviating at -0.4 V$_{RHE}$ to stabilize around 1974 cm^{-1} until it desorbs (Figure 3A). The general trend of the CO peak position decreasing with more cathodic potentials was also observed on other Ag electrodes.[10,32] This shift may be a result of the Stark effect and/or chemical bonding effects due to orbital interactions (donation, back donation, and steric repulsion). Multiple effects may contribute to the field-dependent shift and it is difficult to distinguish the dominant effect.[36] The Stark effect is an interaction of the molecule's dipole with the electric field at the interface, resulting in a change in the vibrational frequency. Chemical bonding effects can influence surface-adsorbed species by altering the charge donation between the metal and the molecular orbitals of the adsorbate as the applied potential is changed.[32,33] A possible explanation for the observed decrease in the CO wavenumber with more negative applied potentials is an increase in the occupancy of the CO antibonding $2\pi^*$ molecular orbital, a chemical bonding effect which would decrease the bond strength.[37] While the mechanism cannot be determined conclusively, we hypothesize that the chemical bonding effect is dominant as CO is expected to be

bound to the surface as a reduction product and density function theory (DFT) has shown this to be the dominant effect at other metal surfaces.[36]

The CO coverage has been quantitatively measured on other metallic electrodes, such as Pt, through electrooxidative stripping, where CO is oxidized to CO_2 around 0.80 V_{RHE}.[31] However, we were unable to quantify the CO coverage in this study because, as described in the In Situ ATR-SEIRAS Measurements section and shown in Figure S3, the greatest anodic potential we could achieve was 0.70 V_{RHE} before the film began to degrade. No CO oxidation peak was ever observed on the anodic scan up to 0.70 V_{RHE} under any conditions. However, the intensity and area of the CO peak does indicate the relative concentration of CO bound to the surface of the Ag cathode. The concentration is relative because in SEIRAS only the sites that experience the surface enhancement result in a strong infrared absorption. The SEIRAS intensity greatly depends on the size, shape, and interparticle spacing of the nanofeatures of the thin film.[38] The nanoparticles must be smaller than the wavelength of visible light and the largest enhancement is obtained when they are aggregated very densely with small gaps in between.[23] Interestingly, plasmonic properties also depend on the size, shape, and density of nanofeatures.[39] While there is no guarantee that the SEIRAS active sites are also the plasmonically active sites, this similarity in enhancement related to nanofeatures increases the likelihood. It is also possible that the sites that exhibit SEIRAS enhancement are not the electrochemically active sites. However, as we are detecting CO, a CO_2 reduction product, it is clear that we are probing at least one electrochemically relevant active site.

The positive direction of the peak signifies that the CO concentration at the surface is greater than the concentration during the background scan at 0.2 V_{RHE} (which is expected to be zero). The CO peak area increases rapidly during the cathodic scan but is fairly constant on the anodic scan, only beginning to decrease after -0.3 V_{RHE} before being completely removed around 0.20 V_{RHE} (Figure 3D). This trend of CO remaining adsorbed on the surface is

somewhat unexpected for Ag, which is generally described as having a low affinity for CO. [40] However, a recent theoretical prediction of CO binding strength on Ag clusters found the adsorption energy to be much higher, close to that of Cu surfaces. [41] In this study CO is even shown to remain on the surface after the applied potential is removed. After CA at -0.6 V_{RHE} for 90 seconds the applied potential was stopped and the system was monitored during OCV. The normalized surface area of the CO peak during OCV decreased for 10 minutes before all of the CO was fully desorbed (Figure 4A). The open circuit potential started at 0.22 V_{RHE} and stabilized at 0.245 V_{RHE} after 10 minutes, corresponding to the complete desorption of CO (Figure S14B).

Performing these same CV scans under constant illumination was possible but resulted in a 10 °C increase in the temperature of the electrolyte during the 20 minute experiment. Increasing the electrolyte temperature decreases the solubility of CO_2 and can change the product distribution as each reaction rate constant will change per the Arrhenius equation. Therefore, it is important to perform dark and illuminated experiments at the same temperature. CA experiments were conducted for 90 seconds in the dark and under constant illumination from the 365 nm LED light source (125 mW cm^{-2}) at -0.2, -0.3, -0.4, -0.5, -0.6, and -0.7 V_{RHE} (Figure S13 and Figure 6). While no area trends can be discerned from this technique, the peak positions can be compared. The CO peak position shifted from 1983 to 1964 cm^{-1} as the potential increased cathodically from -0.4 to -0.7 V_{RHE} in both the dark and in the light (Figure S13A). The overlapping error bars show there is no statistical difference between the CO peak positions under dark or illuminated conditions. This indicates that the plasmonic effect is not influencing the strength of the CO bond by changing its binding orientation or by changing the electronic coupling with Ag.

In prior work we observed that the apparent onset potential for CO_2 reduction to CO was reduced by 300 mV in the light compared to the dark. [3] The total current density in the light begins to increase at -0.2 V_{RHE} while the total current density in the dark only begins
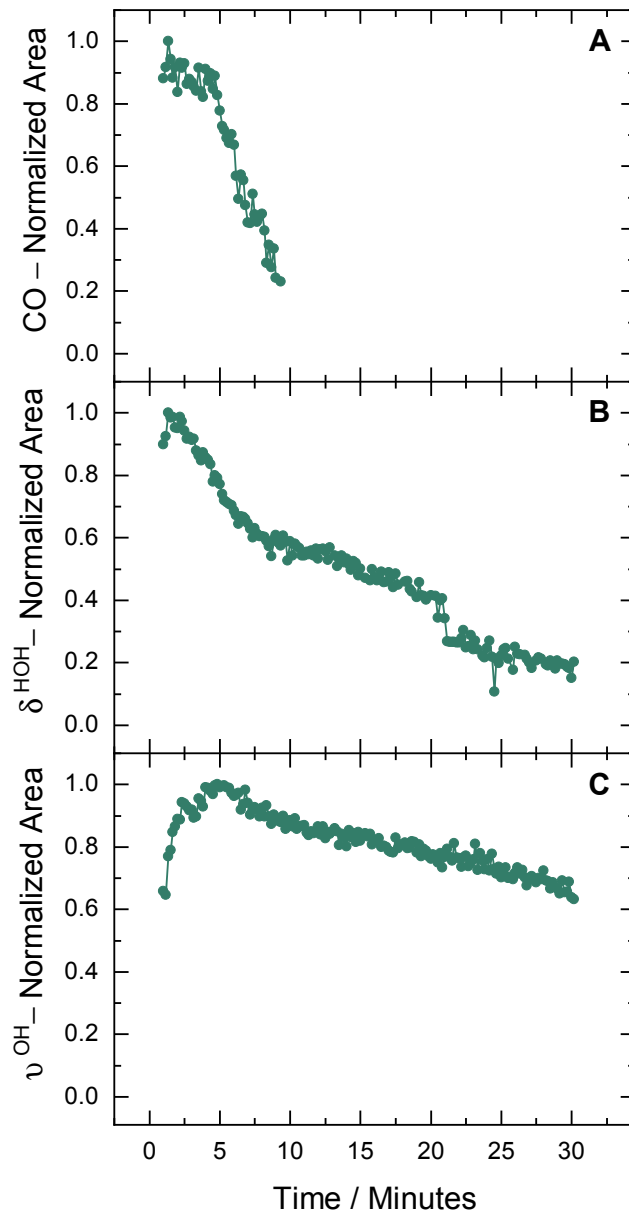
16

Figure 4: Normalized area of three SEIRAS peaks during open circuit relaxation: CO (A), δ^{HOH} (B), and ν^{OH} (C). The area is normalized by the largest area of each peak. The system was allowed to relax at open circuit after CA at -0.6 V_{RHE} for 90 seconds. The activated Ag cathode on a Ge ATR crystal was in 0.1 M KHCO$_3$ with continuous CO$_2$ flow through the electrolyte. Figure S14 shows the SEIRAS scans and open circuit potential corresponding to these plots.

to increase at -0.5 V_{RHE}. Product analysis at -0.37 V_{RHE} confirmed that the only product being produced in the light was CO and no products were detected in the dark. To confirm this observation, CA was performed at -0.2, -0.25, and -0.3 V_{RHE} with SEIRAS spectra

taken at a higher resolution to pinpoint the onset of CO adsorption in the light and in the dark. Figure 5A shows the SEIRAS spectra during constant illumination; no CO peak is observed at -0.2 V_{RHE}, a small CO peak begins to appear at -0.25 V_{RHE}, and a CO peak is clearly visible at -0.3 V_{RHE}. The appearance of the CO peak exactly coincides with the onset of Faradaic cathodic current under 365 nm illumination, implying that, under illuminated conditions, CO is able to desorb at potentials close to where it initially forms on the Ag surface, hence resulting in a measured Faradaic current.
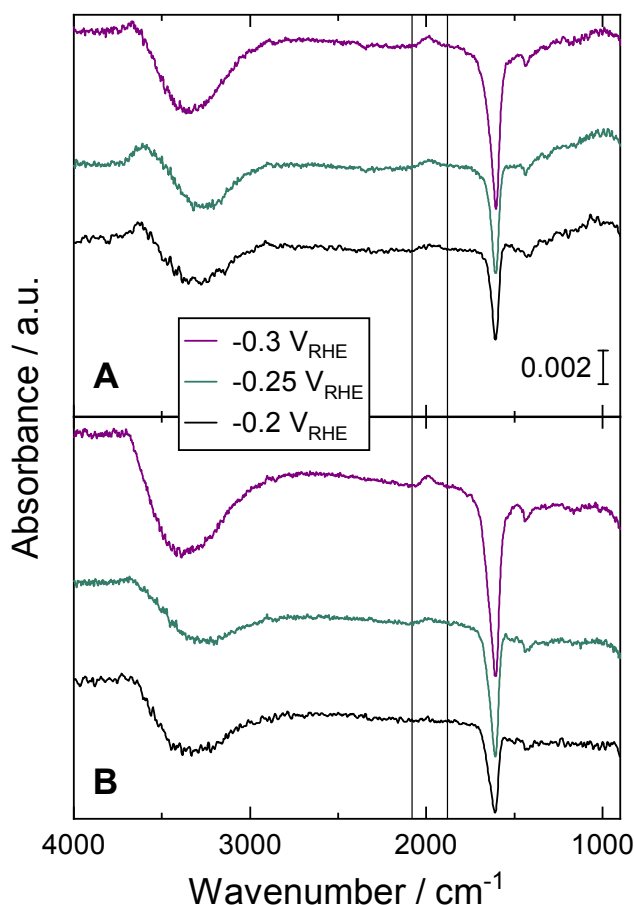

Figure 5: SEIRAS spectra taken during CA at -0.2, -0.25, and -0.3 V_{RHE}. (A) shows the spectra taken under 365 nm LED illumination (125 mW cm^{-2}) and (B) shows the spectra taken in dark conditions. The two vertical lines frame the CO peak position. The activated Ag cathode on a Ge ATR crystal was in 0.1 M KHCO$_3$ with continuous CO$_2$ flow through the electrolyte. The background spectrum was taken at 0.2 V_{RHE}. The scale bar in (A) gives the y-axis scale in absorbance units (a.u.) and applies to both (A) and (B).

Figure 5B shows the high resolution SEIRAS spectra in the dark during CA with the same

range of applied potentials. Surprisingly, the results in the dark are identical to those in the light, indicating that the onset potential of CO_2 reduction to CO in the dark is also -0.25 V_{RHE}, although the desorption of CO (and resulting measured current) under dark conditions is not observed until potentials more cathodic than -0.5 V_{RHE}. This finding reveals that the plasmonic effect induced by the light is enabling the desorption of CO from the surface, making more active sites available for the further reduction of CO_2 to CO. This explains why we observe CO production and a higher current density at these low overpotentials in the light and not the dark.

A possible explanation for the plasmonic mechanism enhancing CO desorption is that energy from plasmonically excited charge-carriers could be dissipating into the lattice, resulting in localized heating of the cathode surface.[42] This increase in temperature could enable the desorption of CO from the Ag surface, which has been shown to occur around 40 °C in gas-phase conditions.[43] However, in our previous studies we showed that plasmonic heating was not the cause of enhanced CO_2 reduction at the Ag cathode because the photocurrent increases linearly with light intensity[3] and increasing the electrolyte temperature from 22 to 35 °C results in a decrease in CO production.[21]

Another explanation for plasmon-enhanced CO desorption is, broadly, the transfer of energized charge-carriers from the Ag to the surface-adsorbed CO. The LSPR can relax through non-radiative excitation of energetic charge-carriers, resulting in the formation of energetic electron-hole pairs at the cathode surface. The strong local electric fields generated during LSPR also promote higher rates of this process.[44] While the enhanced electric field can also affect the binding strength and orientation of adsorbed molecules we see no change in the CO peak position upon illumination at any applied potential (Figure S13C).

In the desorption induced by electronic transitions (DIET) mechanism, the excited electron at the Ag surface can temporarily transfer to partially-occupied or unoccupied molecular orbitals of an adsorbed species, forming an excited metal-adsorbate complex with a different

19

potential energy surface (PES). While on this new PES, the energy of the donated charge carrier is converted into kinetic energy of the metal-adsorbate complex. After a few femtoseconds the donated electron decays back to the metal Fermi level and the adsorbate returns to the ground state PES. If the energy transfer exceeds the activation barrier for desorption, the adsorbate will leave the surface.[39] This mechanism has been invoked for NO,[45] CO,[46,47] and H_2[48] desorption from metal surfaces under vacuum. The DIET mechanism can also be reframed as a *reaction* induced by electronic transitions, where a reaction intermediate adsorbed on the surface overcomes the activation barrier for the reaction to occur. Reports of this mechanism include H_2 dissociation,[49] O_2 dissociation,[50] and C–O bond dissociation.[51]

Water Bend and Stretch

We observe the water bending, δ^{HOH}, signal in the range of 1597–1623 cm^{-1} with an average value of 1600 cm^{-1} (Table 1). This matches well with other reports of the HOH stretch on Ag in electrochemical conditions: 1608 cm^{-1} in 0.05 M Na_2SO_4 at -0.2 V_{RHE} for seven monolayers of Ag over Pt[10] and 1635 cm^{-1} in 0.1 M KCl at -0.85 V_{RHE} on a sputtered Ag thin film.[11] The other water peak observed in this study, the water stretching peak, ν^{OH}, appears in the range of 3351–3520 cm^{-1} with an average value of 3402 cm^{-1} (Table 1). A broad peak centered at 3300 cm^{-1} and spanning this range was also reported for Ag(100) at -0.2 V_{RHE} in 0.1 M NaF.[29] In fact, the regions observed for both the δ^{HOH} and ν^{OH} peaks on Ag are also the typical range for those peaks on other metals, such at Pt,[31] Cu,[10] and Au.[30]

In acidic media it is possible to see a hydronium cation (H_3O^+) bending peak at a higher wavenumber than the δ^{HOH} peak. For example, H_3O^+ peaks were reported at 1758 cm^{-1} at 0.4 V_{RHE} in 0.5 M H_2SO_4 for Pt(111)[52] and 1730 cm^{-1} at 0.2 V_{RHE} in 5 M H_2SO_4 for Au(111).[30] However, in this study no peaks were observed in the H_3O^+ bending region, which is unsurprising as the electrolyte solution was at a pH of 6.8. In basic electrolyte a broad

hydroxide anion (OH^-) stretching peak may be observed as a higher frequency shoulder or component of the ν^{OH} peak. A hydroxide peak was reported at 3480 cm^{-1} as a feature in the high frequency range of the broad water peak from 3100–3500 cm^{-1} (0.2 V_{RHE} in 0.1 M NaOH on a Au film).[53] In this study the ν^{OH} peak is broad and asymmetrical, but no clear features emerge that could be attributed to hydroxide. This is expected in near-neutral electrolyte, although the local pH is expected to increase at the surface of a cathode where CO_2 reduction is occurring as a result of proton consumption.[13]

The δ^{HOH} peak position begins at 1623 cm^{-1} and shifts rapidly to 1599 cm^{-1} during the cathodic scan from 0 to -0.5 V_{RHE} (Figure 3B). For the remainder of the cathodic scan the peak position is constant at 1598 cm^{-1}. On the anodic scan the peak position is identical to the cathodic scan from -0.9 to -0.5 V_{RHE}. Then the peak position begins to increase, but only incrementally, reaching a maximum of 1605 cm^{-1} at 0.4 V_{RHE}. A small positive shoulder around 1630 cm^{-1} in the negative-going δ^{HOH} peak that appears and disappears near -0.6 V_{RHE} is attributed to HCO_3^- and will be discussed in the Carbonate, Bicarbonate, and CO_2 section.

The ν^{OH} peak position shifts quickly from 3427 to 3373 cm^{-1} on the cathodic scan from -0.3 to -0.5 V_{RHE} and essentially stabilizes for the remainder of the cathodic scan at 3375 cm^{-1} (Figure 3C). On the anodic scan the peak positions are identical from -0.9 to -0.5 V_{RHE}. Then the peak position begins to increase again for potentials more anodic than -0.5 V_{RHE}, with values similar to the cathodic scan, reaching 3439 cm^{-1} at 0.2 V_{RHE}.

The wide range of peak positions, large error bars, and broad peak shape of the ν^{OH} feature reflects the many different types and orientations of water and hydroxide that contribute to this peak. The different types of contributing molecules include surface-bound water and OH^-, free water and OH^-, and water associated with anions.[29] All of these contributors have both symmetric and asymmetric stretching vibrations as well as different degrees of hydrogen bonding, both of which can shift the peak position. For example, the asymmetric

stretch of non-bonded water has a higher frequency than the symmetric stretch. A higher degree of hydrogen bonding lowers the wavenumber of the OH stretch while less hydrogen bonding raises it. In addition, species may experience a Stark effect or chemical bonding effect shift with changes in applied potential. For this reason we will not interpret the peak shifts described above as resulting from any one phenomena, as it likely represents a complicated array of changes from each of the different types of molecules present at the surface.

However, we can use the area trends of the ν^{OH} and δ^{HOH} peaks to understand how the EDL structure is changing during conditions relevant to CO_2 reduction. The intensity of the δ^{HOH} and ν^{OH} water peaks is an indication of the average orientation of the first layer of water molecules at the electrode surface. At the potentials more negative than the pzc the water molecules are oriented H-down.[28] As they pass through the pzc the water molecules become oriented with H parallel to the electrode surface and just above the pzc they form an ice-like structure by hydrogen-bonding with water molecules in the second layer.[54] At potentials more positive than the pzc the water molecules are oriented O-down. The density of water at the surface is at a minimum near the pzc and increases with the magnitude of the applied voltage.[28] We can now use this understanding of water reorientation in the EDL to interpret the peak area trends for the δ^{HOH} and ν^{OH} water peaks.

In CO_2 reduction, the relevant region of interest is at potentials more negative than the pzc. The pzc for Ag(100) was -0.2 V_{RHE} in 0.1 M NaF and 0.1 M KF[29] and the pzc for Ag(111) was -0.07 V_{RHE} in 0.1 M NaF.[28] In this region for both δ^{HOH} and ν^{OH} we see the peak area increase with more cathodic potentials until it stabilizes at -0.8 V_{RHE} (Figure 3E and F). This indicates that the water molecules at the surface are reorienting to be more H-down, perhaps reaching the maximum orientation at -0.8 V_{RHE}. On the anodic scan, the peak area is constant (δ^{HOH}) or even increasing slightly (ν^{OH}) until 0.3 V_{RHE}.

Clearly on the anodic scan, the EDL structure is not the same as it was on the cathodic

scan. It seems once the water molecules are oriented H-down they stay in that position beyond where we might expect the pzc to be. This resistance to change in the average water molecule orientation can also be seen in the OCV behavior (Figure 4B and C). After 90 seconds of CA at -0.6 V_{RHE} the δ^{HOH} and ν^{OH} peak areas decrease slowly over the course of 30 minutes. While the open circuit potential changes from 0.22 to 0.245 V_{RHE} within the first 10 minutes, the potential is stable for the remaining 20 minutes (Figure S14B). As described above, these peaks, and thus the EDL structure, will eventually reach a steady state over the course of one to two hours. We also observe during longer CA experiments that the EDL structure changes rapidly during the first 5–10 minutes, with the δ^{HOH} and ν^{OH} peak areas increasing sharply (Figure S15). After this initial region, the rate of peak area change slows down considerably although still continues to increase. This implies that CO_2 reduction experiments performed in the first 5–10 minutes of applied potential may have different results than longer experiments due to differences in the EDL structure. The dense, close-packed layer of water that eventually forms at the surface of a charged electrode is thought to be favorable for rapid proton transfer[55] which would impact the partial current densities towards H_2 production and all CO_2 reduction products.

Above 0.3 V_{RHE} the peak area of δ^{HOH} drops suddenly while scanning anodically. As described previously and shown in Figure 1 there are potential regions where the δ^{HOH} peak has a positive and negative component. δ^{HOH} peaks with this same shape have been reported during potential scans at Pt[31] and Au[30,54] surfaces. This rapid peak area decrease corresponds to the region in the anodic scan where the peak again has a positive and negative component before finally becoming a positive peak around 0.6 V_{RHE} (Figure S11. Near this same potential on the anodic scan the ν^{OH} peak flips from negative to positive. This behavior is interpreted as the shift from H-down to O-down water orientation at the surface, where the positive and negative δ^{HOH} peak components likely result from this reorientation. Similarly, the initial region where the δ^{HOH} peak has both a positive and negative component and where the peak position decreases rapidly reflects the reorientation of water to the

H-down position.

Carbonate, Bicarbonate, and CO$_2$

While there are no reports of HCO_3^- or CO_3^{2-} species at biased Ag electrodes in aqueous electrolyte, there are several IR spectroscopy reports of these species in aqueous solutions.[56–59] There are many IR-active modes of both HCO_3^- and CO_3^{2-} with several appearing in the fingerprint region.[58] Here we will focus on the HCO_3^- and CO_3^{2-} peaks that may appear above 1100 cm^{-1}. For HCO_3^- these modes are the COH bend (δ^{COH}) near 1300–1320 cm^{-1};[56,58,59] the symmetric CO$_2$ stretch ($\nu_s^{CO_2}$) around 1355–1364 cm^{-1}, which is commonly seen as the most intense peak;[56,58,59] and the asymmetric CO$_2$ stretch ($\nu_{as}^{CO_2}$) near 1620–1634 cm^{-1}, which in this study would overlap with δ^{HOH}.[56,58] There is one IR-active mode for CO_3^{2-} above 1100 cm^{-1}: the asymmetric stretch ($\nu_{as}^{CO_3^{2-}}$) around 1374–1396 cm^{-1}, which is typically the most intense peak.[56–59] While these studies report a single average peak position for each mode, they acknowledge that the assignments are approximate because there can be coupling between the modes and the peak positions vary with the solution composition and concentration.[58]

In addition to these reports of HCO_3^- and CO_3^{2-} in aqueous solutions there is also an IR spectroscopy study of gas-phase $HCO_3^-(H_2O)_{1-10}$ clusters.[60] They found that the HCO_3^- peak positions increased with increasing water coordination, except for the peak which overlaps with δ^{HOH}.[60] They reported the δ^{COH} mode from 1177–1205 cm^{-1}, the $\nu_s^{CO_2}$ mode at 1288–1353 cm^{-1}, and the $\nu_{as}^{CO_2}$ mode from 1653–1706.[60] Finally, there are two IR spectroscopy studies of HCO_3^- and CO_3^{2-} species at biased metallic electrodes in aqueous electrolyte.[12,31] Iwasita et al. reported adsorbed HCO_3^- at 1330 cm^{-1} and adsorbed CO_3^{2-} at 1400 cm^{-1} at a positively biased (0.6–0.9 V$_{RHE}$) Pt(111) electrode in CO$_2$-saturated 0.1 M HClO$_4$.[31] Dunwell et al. observed a HCO_3^- peak at 1362 cm^{-1} and a CO_3^{2-} peak at 1402 cm^{-1} at a

negatively biased (-0.9 V_{RHE}) Au film in 1.0 M NaHCO$_3$.[12]

In this study we observe two peaks in the 1100–1500 cm^{-1} region: a peak from 1276–1279 cm^{-1} with an average value of 1278 cm^{-1} and a peak at 1393–1401 cm^{-1} with an average value of 1395 cm^{-1}. We attribute the peak at 1395 cm^{-1} to the $\nu_{as}^{CO_3^{2-}}$ mode as the position is consistent with reports of CO_3^{2-} in aqueous solutions[56–59] and at biased metallic electrodes in aqueous electrolyte.[12,31] The peak at 1278 cm^{-1} is a little lower than expected for the dominant HCO_3^- $\nu_s^{CO_2}$ mode[12,31,56,58,59] or the δ^{COH} mode.[56,58,59] However, in all reports the HCO_3^- modes always appear at a lower wavenumber than the $\nu_{as}^{CO_3^{2-}}$ mode.[12,31,56–60] In addition, the HCO_3^- $\nu_s^{CO_2}$ in the hydrated gas phase was reported from 1288–1353 cm^{-1},[60] very close to our observed peak at 1276–1279 cm^{-1}. The explanation for the lower wavenumber was less water coordination,[60] which could certainly occur close to the negatively biased Ag cathode where water is highly oriented.[28] While two peaks are expected for formate at 1350 and 1383 cm^{-1}, the dominant peak should appear at 1580 cm^{-1}.[61] However, no peak is observed near 1580 cm^{-1} and the concentration of formate, with a Faradaic Efficiency of just 2% at -0.7 V_{RHE},[3] would be five orders of magnitude less than the concentration of HCO_3^-. Finally, a small positive shoulder around 1630 cm^{-1} in the negative-going δ^{HOH} peak appears and disappears at the same potentials as the peak at 1278 cm^{-1} (Figure 1), consistent with the HCO_3^- $\nu_{as}^{CO_2}$ mode.[56,58] Thus, we conclude that the peak we observe at 1278 cm^{-1} is most likely the HCO_3^- $\nu_s^{CO_2}$ mode. Additionally, as we do not expect anions to adsorb to an electrode that is biased to potentials negative of the pzc, we interpret these HCO_3^- and CO_3^{2-} peaks as near-surface species, within 10 nm of the cathode surface.[12,62]

In this study we observed CO_2 as a single peak at 2342 cm^{-1} for all potentials where it appears. The assignment of the CO_2 peak is consistent with several literature reports of CO_2 at biased metallic electrodes in aqueous electrolyte. CO_2 has been observed at 2343 cm^{-1} at a positively biased (0.6–0.9 V_{RHE}) Pt(111) electrode in CO_2-saturated 0.1 M HClO$_4$,[31] at 2340 cm^{-1} at a negatively biased (-0.9 V_{RHE}) Au film in 1.0 M NaHCO$_3$,[53] and at 2345

cm^{-1} in CO$_2$-saturated 0.1 M KCl at -0.9 V$_{RHE}$ on a sputtered Ag thin film.[11]

The average peak positions and normalized areas during cathodic and anodic CV scans for HCO$_3^-$, CO$_3^{2-}$, and CO$_2$ peaks are shown in Figure S12. The trends are remarkably similar; all three peaks appear and disappear around -0.6 V$_{RHE}$ (Table S1). The peak areas increase with more cathodic potentials and decrease on the anodic scan with only slightly larger peak areas than on the cathodic scan. The CO$_2$ position never deviates and the CO$_3^{2-}$ position varies slightly but the generally overlapping error bars show no trend with potential. Only the HCO$_3^-$ peak position changes, increasing with more cathodic potentials with no hysteresis on the anodic scan (Figure S12A and Figure 6). Accordingly, no shift in peak position for HCO$_3^-$, CO$_3^{2-}$, or CO$_2$ was reported from 0.1 to -0.9 V$_{RHE}$ for a polycrystalline Au film.[12] On Pt(111) the HCO$_3^-$ peak position was independent of potential while the CO$_3^{2-}$ peak position increased with more anodic potentials from 0.6 to 0.95 V$_{RHE}$ but, as discussed above, the the orientation and structure of water at the surface of a positively charged electrode is quite different from that of a negatively charged electrode, and the changes in peak position were attributed to shifts in the water orientation.[31]

We consider these three species together because their concentrations are linked by the following reactions (Equation 1 and Equation 2).

$$CO_2 + H_2O \rightleftharpoons H^+ + HCO_3^- \tag{1}$$

$$HCO_3^- \rightleftharpoons H^+ + CO_3^{2-} \tag{2}$$

The peak area trends can be understood through the equilibrium between HCO$_3^-$, CO$_3^{2-}$, and CO$_2$. As the applied cathodic potential increases in magnitude the current density increases due to increasing CO$_2$ reduction and H$_2$ formation rates (Figure S9). As both of these reactions consume protons, equations 1 and 2 shift to the right, converting CO$_2$ at the surface into HCO$_3^-$ and CO$_3^{2-}$. This results first in an increase in the concentration

of HCO_3^- beginning at -0.56 V_{RHE} followed by an increase in the concentration of CO_3^{2-} starting at -0.69 V_{RHE}, as seen through the positive peaks that increase in area (Figure 1 and Figure S12). This also results in a decrease in the concentration of CO_2, which we observe as a negative peak with an increasing area beginning at -0.65 V_{RHE} (Figure 1 and Figure 3). Additionally, the CO_2 concentration will decrease near the surface as it is reduced to form CO and formate, especially as the current density increases and exceeds the mass-transfer rate of CO_2 to the surface. The OH^- concentration will also increase at the cathode surface resulting in an increase in the local pH.[15,63]

When comparing dark and 365 nm illuminated conditions, the IR spectra are very similar for nearly all species discussed in this article, with the lone difference being a shift in the HCO_3^- peak position. As presented in the introduction, our prior study of a plasmonic Ag cathode showed significant differences in the product distribution in the dark and under 365 nm LED illumination.[3] CO production was enhanced and H_2 evolution was suppressed at low overpotentials upon illumination; formate production was enhanced at all overpotentials in the light; and methanol was only formed under illuminated conditions at potentials more cathodic than -0.8 V_{RHE}.[3] In this study we performed both CV and CA experiments under 365 nm LED illumination but we observed very few differences between SEIRAS spectra in the light and the dark. No methanol (1470 and 2970 cm^{-1})[64] or formate (1350, 1383, and 1581 cm^{-1})[61] peaks were observed in the light or the dark at any potential. As the expected methanol Faradaic efficiency at -0.8 and -0.9 V_{RHE} is 0.1% and 0.4% respectively,[3] it is possible that the methanol concentration at the surface was below the detection limit of the IR spectrometer. Due to stability issues with the Ag thin film at potentials more cathodic than -0.9 V_{RHE} we were unable to study the potential regions with higher methanol Faradaic efficiencies.

As previously discussed, the onset of CO formation in the light and the dark was identically -0.25 V_{RHE} (Figure 5). Figure S13 shows there is no difference between the light and dark

average peak positions for CO_2, CO, ν^{OH}, or δ^{HOH} during 90 seconds of CA at any potential from -0.2 to -0.7 V_{RHE}. CO_3^{2-} is not plotted because there is insufficient data for this peak in this potential range. Surprisingly, the only measureable difference between the illuminated and dark cathode is the HCO_3^- peak position, which increases by approximately 6 cm^{-1} under illumination at -0.5, -0.6, and -0.7 V_{RHE} (Figure 6). This 6 cm^{-1} increase in position can also be observed when the system was allowed to stabilize in the dark at -0.5 V_{RHE} for 20 minutes before rapidly turning on the light source. The change was observed in the first spectrum taken in the light (10 seconds) before any heating could occur. This peak shift was also accompanied by an immediate increase in the peak area.
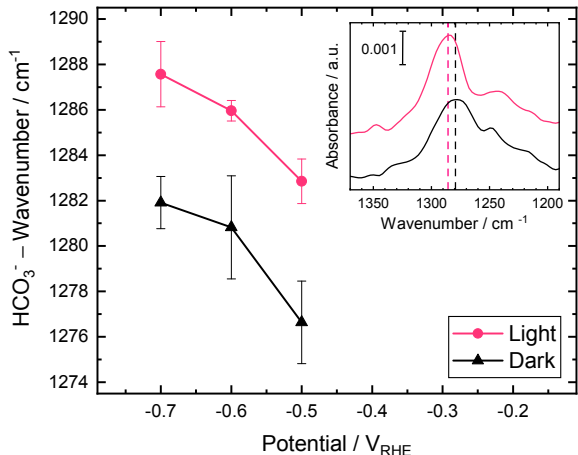

Figure 6: Average position of the HCO_3^- peak during CA for 90 seconds at -0.5, -0.6, and -0.7 V_{RHE} in the dark (black) and under 365 nm LED illumination (125 mW cm^{-2}) (pink). Average values and standard deviations are calculated from 2–5 CA experiments at each applied potential. Experiments were performed on different days with a new cathode prepared each day. Error bars represent one standard deviation. The inset shows two representative spectra in the dark and light at -0.6 V_{RHE}. The activated Ag cathode on a Ge ATR crystal was in 0.1 M KHCO$_3$ with continuous CO_2 flow through the electrolyte. The background spectrum was taken at 0.2 V_{RHE}. The inset scale bar gives the y-axis scale in absorbance units (a.u.).

An increase in the HCO_3^- peak position signifies an increase in the strength of the bond. As no other immediate changes are apparent between the dark and light spectra, we can conclude that this increase in the HCO_3^- bond strength is not caused by changes in the other species we observe at the surface. In the potential range of -0.5 to -0.7 V_{RHE} where

this change occurs we know that CO production will be enhanced, H_2 evolution will be suppressed, and at -0.7 V_{RHE} formate production will be enhanced in the light (Figure S8 and Figure S9).[3] An increase in the concentration of HCO_3^- near the surface would raise the local pH which would lead to enhancement in CO_2 reduction and diminished H_2 evolution.[65]

The Raman shift of a probe molecule (4-methoxyphenyl isocyanide) on Au core Pt shell nanoparticles upon illumination at the plasmon resonance frequency (530 nm) was used by Yang et al. to determine the surface temperature. They found that the peak position decreased linearly with increasing temperature, which they attributed to a weakening of the interaction between the molecule and the substrate, allowing the molecules to reorient. Similarly, we find that the HCO_3^- peak position continues to increase linearly over time under constant illumination, which corresponds to a linear increase in temperature. However, they showed that the peak position did not change upon illumination until 50 seconds had elapsed.[66] Therefore we conclude that the immediate HCO_3^- peak shift we observe within the first 10 seconds of illumination is not caused by a temperature rise at the surface. We hypothesize that the observed increase in the peak position upon illumination is due to interactions of HCO_3^- molecules with the enhanced local electric field generated by the plasmon resonance, similar to the observed increase in peak position in the dark due to the electric field generated by the applied voltage (Stark effect).

Although CO also experiences a shift in peak position in the dark, there is no change in the wavenumber upon illumination (Figure S13C). We would expect a shift in the CO peak position in the light similar to that of HCO_3^- if the change in the dark was due to the Stark effect. However, if the CO shift in the dark is due to the chemical bonding effect, we would not expect an additional shift with a plasmonically enhanced local electric field.

Conclusions

We used in situ ATR-SEIRAS to probe the species at the surface of a plasmonic Ag cathode during CO_2 reduction in both the dark and under illumination. The SEIRAS signal can be enhanced while still maintaining cathode stability by optimizing the deposition conditions and through electrochemical CV cycling. We observe peaks for HCO_3^- (1278 cm^{-2}), CO_3^{2-} (1395 cm^{-2}), δ^{HOH} (1600 cm^{-2}), CO (1970 cm^{-2}), CO_2 (2342 cm^{-2}), and ν^{OH} (3402 cm^{-2}) under a range of applied potentials relevant to CO_2 reduction. Trends in the water δ^{HOH} and ν^{OH} peaks show that the water reorientation at the charged electrode surface can be slow to stabilize and slow to return to the original orientation. It is therefore important to "reset" the EDL by an anodic scan during SEIRAS to ensure that experimental results are repeatable. In addition, experiments considering product distribution should wait until the EDL has stabilized (approximately 5–10 minutes) before conducting product analysis.

We find that CO remains on the Ag surface until an anodic potential of 0.20 V_{RHE} is reached or after 10 minutes during OCV relaxation. Despite current density trends showing a decrease in the overpotential for CO formation upon illumination, we find that the onset of CO_2 reduction to CO is identical in the light and the dark (-0.25 V_{RHE}). We conclude that the light must be assisting the desorption of CO from the surface, possibly through a DIET mechanism induced by excited electrons generated through LSPR relaxation.

Finally, we confirm the expected increase in local pH at higher current densities through the changing concentrations of HCO_3^-, CO_3^{2-}, and CO_2 at the surface. The only change between spectra in the light and the dark is the immediate increase in the HCO_3^- wavenumber and peak area upon illumination. We propose that the enhanced local electric field that results from the LSPR is strengthening the HCO_3^- bond, further increasing the local pH. While the exact mechanism of plasmon-enhanced CO_2 reduction at a Ag surface is still uncertain, this in situ ATR-SEIRAS study sheds some light on how H_2 evolution is suppressed while CO_2

reduction is promoted at an illuminated Ag cathode.

Associated Content

Schematics, cathode activation, cathode characterization, product analysis, and additional SEIRAS spectra and analysis of SEIRAS peak position and area with potential, time, and illumination conditions.

Author Information

Corresponding Author

*bmcclosk@berkeley.edu

*r.kortlever@tudelft.nl

ORCID

Bryan D. McCloskey: 0000-0001-6599-2336 Ruud Kortlever: 0000-0001-9412-7480

Notes

The authors declare no competing financial interest.

Acknowledgement

References

(1) De Luna, P.; Hahn, C.; Higgins, D.; Jaffer, S. A.; Jaramillo, T. F.; Sargent, E. H. What would it take for renewably powered electrosynthesis to displace petrochemical processes? *Science* **2019**, *364*.

(2) Kim, Y.; Creel, E. B.; Corson, E. R.; McCloskey, B. D.; Urban, J. J.; Kostecki, R. Surface-plasmon-assisted photoelectrochemical reduction of CO_2 and NO_3^- on nanostructured silver electrodes. *Adv. Energy Mat.* **2018**, *8*, 1800363.

(3) Creel, E. B.; Corson, E. R.; Eichhorn, J.; Kostecki, R.; Urban, J. J.; McCloskey, B. D. Directing selectivity of electrochemical carbon dioxide reduction using plasmonics. *ACS Energy Lett.* **2019**, *4*, 1098–1105.

(4) Zheng, Z.; Xie, W.; Li, M.; Ng, Y. H.; Wang, D.-W.; Dai, Y.; Huang, B.; Amal, R. Plat-

inum electrocatalysts with plasmonic nano-cores for photo-enhanced oxygen-reduction. *Nano Energy* **2017**, *41*, 233–242.

(5) Shi, F.; He, J.; Zhang, B.; Peng, J.; Ma, Y.; Chen, W.; Li, F.; Qin, Y.; Liu, Y.; Shang, W.; Tao, P.; Song, C.; Deng, T.; Qian, X.; Ye, J.; Wu, J. Plasmonic-enhanced oxygen reduction reaction of silver/graphene electrocatalysts. *Nano Lett.* **2019**, *19*, 1371–1378.

(6) Zhang, H. X.; Li, Y.; Li, M. Y.; Zhang, H.; Zhang, J. Boosting electrocatalytic hydrogen evolution by plasmon-driven hot-electron excitation. *Nanoscale* **2018**, *10*, 2236–2241.

(7) Guo, X.; Li, X.; Kou, S.; Yang, X.; Hu, X.; Ling, D.; Yang, J. Plasmon-enhanced electrocatalytic hydrogen/oxygen evolution by Pt/Fe–Au nanorods. *J. Mater. Chem. A* **2018**, *6*, 7364–7369.

(8) Wilson, A. J.; Mohan, V.; Jain, P. K. Mechanistic understanding of plasmon-enhanced electrochemistry. *J. Phys. Chem. C* **2019**, *123*, 29360–29369.

(9) Hatsukade, T.; Kuhl, K. P.; Cave, E. R.; Abram, D. N.; Jaramillo, T. F. Insights into the electrocatalytic reduction of CO_2 on metallic silver surfaces. *Phys. Chem. Chem. Phys.* **2014**, *16*, 13814–13819.

(10) Oda, I.; Ogasawara, H.; Ito, M. Carbon monoxide adsorption on copper and silver electrodes during carbon dioxide electroreduction studied by infrared reflection absorption spectroscopy and surface-enhanced raman spectroscopy. *Langmuir* **1996**, *12*, 1094–1097.

(11) Firet, N. J.; Smith, W. A. Probing the reaction mechanism of CO_2 electroreduction over Ag films via operando infrared spectroscopy. *ACS Catal.* **2017**, *7*, 606–612.

(12) Dunwell, M.; Yang, X.; Setzler, B. P.; Anibal, J.; Yan, Y.; Xu, B. Examination of near-

electrode concentration gradients and kinetic impacts on the electrochemical reduction of CO_2 using surface-enhanced infrared spectroscopy. *ACS Catal.* **2018**, *8*, 3999–4008.

(13) Gattrell, M.; Gupta, N.; Co, A. A review of the aqueous electrochemical reduction of CO_2 to hydrocarbons at copper. *J. Electroanal. Chem.* **2006**, *594*, 1–19.

(14) Gunathunge, C. M.; Li, X.; Li, J.; Hicks, R. P.; Ovalle, V. J.; Waegele, M. M. Spectroscopic observation of reversible surface reconstruction of copper electrodes under CO_2 reduction. *J. Phys. Chem. C* **2017**, *121*, 12337–12344.

(15) Yang, K.; Kas, R.; Smith, W. A. In situ infrared spectroscopy reveals persistent alkalinity near electrode surfaces during CO_2 electroreduction. *J. Am. Chem. Soc.* **2019**, *141*, 15891–15900.

(16) Kas, R.; Ayemoba, O.; Firet, N. J.; Middelkoop, J.; Smith, W. A.; Cuesta, A. In-situ infrared spectroscopy applied to the study of the electrocatalytic reduction of CO_2: Theory, practice and challenges. *ChemPhysChem* **2019**, *20*, 2904–2925.

(17) Sato, S.; Ueda, K.; Kawasaki, Y.; Nakamura, R. In situ IR observation of surface species during the photocatalytic decomposition of acetic acid over TiO_2 films. *J. Phys. Chem. B* **2002**, *106*, 9054–9058.

(18) Nakamura, R.; Nakato, Y. Primary intermediates of oxygen photoevolution reaction on TiO_2 (rutile) particles, revealed by in situ FTIR absorption and photoluminescence measurements. *J. Am. Chem. Soc.* **2004**, *126*, 1290–1298.

(19) Zandi, O.; Hamann, T. W. Determination of photoelectrochemical water oxidation intermediates on haematite electrode surfaces using operando infrared spectroscopy. *Nat. Chem.* **2016**, *8*, 778–783.

(20) Ekstrom, G. N.; McQuillan, A. J. In situ infrared spectroscopy of glyoxylic acid ad-

sorption and photocatalysis on TiO_2 in aqueous solution. *J. Phys. Chem. B* **1999**, *103*, 10562–10565.

(21) Corson, E. R.; Creel, E. B.; Kim, Y.; Urban, J. J.; Kostecki, R.; McCloskey, B. D. A temperature-controlled photoelectrochemical cell for quantitative product analysis. *Rev. Sci. Instrum.* **2018**, *89*, 055112.

(22) Kuhl, K. P.; Cave, E. R.; Abram, D. N.; Jaramillo, T. F. New insights into the electrochemical reduction of carbon dioxide on metallic copper surfaces. *Energy Environ. Sci.* **2012**, *5*, 7050–7059.

(23) Nishikawa, Y.; Nagasawa, T.; Fujiwara, K. Silver Island Films for Surface-Enhanced Infrared Absorption Spectroscopy: Effect of Island Morphology on the Absorption Enhancement. *Vib. Spectrosc.* **1993**, *6*, 43–53.

(24) Delgado, J. M.; Orts, J. M.; Rodes, A. A comparison between chemical and sputtering methods for preparing thin-film silver electrodes for in situ ATR-SEIRAS studies. *Electrochim. Acta* **2007**, *52*, 4605–4613.

(25) Chandra, R.; Taneja, P.; John, J.; Ayyub, P. Synthesis and TEM study of nanoparticles and nanocrystalline thin films of silver by high pressure sputtering. *Nanostruct. Mater.* **1999**, *11*, 1171–1179.

(26) Del Re, M.; Gouttebaron, R.; Dauchot, J.; Leclère, P.; Lazzaroni, R.; Wautelet, M.; Hecq, M. Growth and morphology of magnetron sputter deposited silver films. *Surf. Coat. Tech.* **2002**, *151*, 86–90.

(27) Zippel, E.; Breiter, M. W.; Kellnert, R. Fourier-transform infrared, attenuated total reflection spectroscopy: A complementary tool for the investigation of the adsorption of CO on thin metal layers. *J. Chem. Soc. Faraday Trans.* **1991**, *87*, 637–642.

(28) Toney, M. F.; Howard, J. N.; Richer, J.; Borges, G. L.; Gordon, J. G.; Melroy, O. R.; Wieslert, D. G.; Vee, D.; Sorensen, L. B. Voltage-dependent ordering of water molecules at an electrode-electrolyte interface. *Nature* **1994**, *368*, 444–446.

(29) Schultz, Z. D.; Shaw, S. K.; Gewirth, A. A. Potential Dependent Organization of Water at the Electrified Metal-Liquid Interface. *J. Am. Chem. Soc.* **2005**, *127*, 15916–15922.

(30) Ataka, K.-i.; Osawa, M. In Situ Infrared Study of Water-Sulfate Coadsorption on Gold(111) in Sulfuric Acid Solutions. *Langmuir* **1998**, *14*, 951–959.

(31) Iwasita, T.; Nart, F. C. In situ infrared spectroscopy at electrochemical interfaces. *Prog. Surf. Sci.* **1997**, *55*, 271–340.

(32) Ikezawa, Y.; Saito, H.; Matsubayashi, H.; Toda, G. Comparative study of CO adsorbed on Pt, Pd, Au and Ag electrodes in neutral solution by IR reflection absorption spectroscopy. *J. Electroanal. Chem* **1988**, *252*, 395–402.

(33) Bewick, A. In-situ infrared spectroscopy of the electrode/electrolyte solution interphase. *J. Electroanal. Chem.* **1983**, *150*, 481–493.

(34) Dunwell, M.; Wang, J.; Yan, Y.; Xu, B. Surface enhanced spectroscopic investigations of adsorption of cations on electrochemical interfaces. *Phys. Chem. Chem. Phys.* **2017**, *19*, 971–975.

(35) Dunwell, M.; Yang, X.; Yan, Y.; Xu, B. Potential routes and mitigation strategies for contamination in interfacial specific infrared spectroelectrochemical studies. *The Journal of Physical Chemistry C* **2018**, *122*, 24658–24664.

(36) Koper, M. T. M.; van Santen, R. A.; Wasileski, S. A.; Weaver, M. J. Field-dependent chemisorption of carbon monoxide and nitric oxide on platinum-group (111) surfaces: Quantum chemical calculations compared with infrared spectroscopy at electrochemical and vacuum-based interfaces. *J. Chem. Phys.* **2000**, *113*, 4392–4407.

(37) Blyholder, G. Molecular orbital view of chemisorbed carbon monoxide. *J. Phys. Chem.* **1964**, *68*, 2772–2777.

(38) Osawa, M.; Ataka, K.-i. Electromagnetic mechanism of enhanced infrared absorption of molecules adsorbed on metal island films. *Surf. Sci. Lett.* **1992**, *262*, L118–L122.

(39) Linic, S.; Christopher, P.; Ingram, D. B. Plasmonic-metal nanostructures for efficient conversion of solar to chemical energy. *Nat. Mater.* **2011**, *10*, 911–921.

(40) Kuhl, K. P.; Hatsukade, T.; Cave, E. R.; Abram, D. N.; Kibsgaard, J.; Jaramillo, T. F. Electrocatalytic conversion of carbon dioxide to methane and methanol on transition metal surfaces. *J. Am. Chem. Soc.* **2014**, *136*, 14107–14113.

(41) Zhang, X.-G.; Liu, Y.; Zhan, C.; Jin, X.; Chi, Q.; Wu, D.-Y.; Zhao, Y.; Tian, Z.-Q. Reaction selectivity for plasmon-driven carbon dioxide reduction on silver clusters: A theoretical prediction. *J. Phys. Chem. C* **2019**, *123*, 11101–11108.

(42) Qiu, J.; Wei, W. D. Surface plasmon-mediated photothermal chemistry. *J. Phys. Chem. C* **2014**, *118*, 20735–20749.

(43) Qu, Z.; Cheng, M.; Huang, W.; Bao, X. Formation of subsurface oxygen species and its high activity toward CO oxidation over silver catalysts. *J. Catal.* **2005**, *229*, 446–458.

(44) Linic, S.; Aslam, U.; Boerigter, C.; Morabito, M. Photochemical transformations on plasmonic metal nanoparticles. *Nat. Mater.* **2015**, *14*, 567–576.

(45) Prybyla, J. A.; Heinz, T. F.; Misewich, J. A.; Loy, M. M.; Glownia, J. H. Desorption induced by femtosecond laser pulses. *Phys. Rev. Lett.* **1990**, *64*, 1537–1540.

(46) Prybyla, J. A.; Tom, H. W.; Aumiller, G. D. Femtosecond time-resolved surface reaction: Desorption of CO from Cu(111) in <325 fsec. *Phys. Rev. Lett.* **1992**, *68*, 503–506.

(47) Bartels, L.; Meyer, G.; Rieder, K.-H. Dynamics of electron-induced manipulation of individual CO molecules on Cu(111). *Phys. Rev. Lett.* **1998**, *80*, 2004–2007.

(48) Denzler, D. N.; Frischkorn, C.; Hess, C.; Wolf, M.; Ertl, G. Electronic excitation and dynamic promotion of a surface reaction. *Phys. Rev. Lett.* **2003**, *91*, 226102.

(49) Mukherjee, S.; Libisch, F.; Large, N.; Neumann, O.; Brown, L. V.; Cheng, J.; Lassiter, J. B.; Carter, E. A.; Nordlander, P.; Halas, N. J. Hot electrons do the impossible: plasmon-induced dissociation of H_2 on Au. *Nano Lett.* **2013**, *13*, 240–247.

(50) Christopher, P.; Xin, H.; Linic, S. Visible-light-enhanced catalytic oxidation reactions on plasmonic silver nanostructures. *Nat. Chem.* **2011**, *3*, 467–472.

(51) Robatjazi, H.; Zhao, H.; Swearer, D. F.; Hogan, N. J.; Zhou, L.; Alabastri, A.; McClain, M. J.; Nordlander, P.; Halas, N. J. Plasmon-induced selective carbon dioxide conversion on earth-abundant aluminum-cuprous oxide antenna-reactor nanoparticles. *Nat. Commun.* **2017**, *8*, 27.

(52) Hirota, K.; Song, M.-B.; Ito, M. In-situ infrared spectroscopy of water and electrolytes adsorbed on a Pt(111) electrode surface in acid solution. Structural changes of adsorbed water molecules upon an electrode potential. *Chem. Phys. Lett.* **1996**, *250*, 335–341.

(53) Dunwell, M.; Yan, Y.; Xu, B. A surface-enhanced infrared absorption spectroscopic study of pH dependent water adsorption on Au. *Surf. Sci.* **2016**, *650*, 51–56.

(54) Ataka, K.-i.; Yotsuyanagi, T.; Osawa, M. Potential-dependent reorientation of water molecules at an electrode/electrolyte interface studied by surface-enhanced infrared absorption spectroscopy. *J. Phys. Chem.* **1996**, *100*, 10664–10672.

(55) Ito, M.; Yamazaki, M. A new structure of water layer on Cu(111) electrode surface during hydrogen evolution. *Phys. Chem. Chem. Phys.* **2006**, *8*, 3623–3626.

(56) Davis, A. R.; Oliver, B. G. A Vibrational-Spectroscopic Study of the Species Present in the CO_2—H_2O System. *J. Solution Chem.* **1972**, *1*, 329–339.

(57) Oliver, B. G.; Davis, A. R. Vibrational Spectroscopic Studies of Aqueous Alkali Metal Bicarbonate Carbonate Solutions. *Can. J. Chem.* **1973**, *51*, 698–702.

(58) Rudolph, W. W.; Fischer, D.; Irmer, G. Vibrational Spectroscopic Studies and Density Functional Theory Calculations of Speciation in the CO_2—Water System. *Appl. Spectrosc.* **2006**, *60*, 130–144.

(59) Stefánsson, A.; Lemke, K. H.; Bénézeth, P.; Schott, J. Magnesium bicarbonate and carbonate interactions in aqueous solutions: An infrared spectroscopic and quantum chemical study. *Geochim. Cosmochim. Acta* **2017**, *198*, 271–284.

(60) Garand, E.; Wende, T.; Goebbert, D. J.; Bergmann, R.; Meijer, G.; Neumark, D. M.; Asmis, K. R. Infrared Spectroscopy of Hydrated Bicarbonate Anion Clusters: $HCO_3^-(H_2O)_{1-10}$. *J. Am. Chem. Soc.* **2010**, *132*, 849–856.

(61) Rotzinger, F. P.; Kesselman-Truttmann, J. M.; Hug, S. J.; Shklover, V.; Gratzel, M. Structure and Vibrational Spectrum of Formate and Acetate Adsorbed from Aqueous Solution onto the TiO_2 Rutile (110) Surface. *J. Phys. Chem. B* **2004**, *108*, 5004–5017.

(62) Ayemoba, O.; Cuesta, A. Spectroscopic Evidence of Size-Dependent Buffering of Interfacial pH by Cation Hydrolysis during CO_2 Electroreduction. *ACS Appl. Mater. Interfaces* **2017**, *9*, 27377–27382.

(63) Singh, M. R.; Clark, E. L.; Bell, A. T. Effects of electrolyte, catalyst, and membrane composition and operating conditions on the performance of solar-driven electrochemical reduction of carbon dioxide. *Phys. Chem. Chem. Phys.* **2015**, *17*, 18924–18936.

(64) Dai, Q.; Gellman, A. J. A HREELS study of C_1—C_5 straight chain alcohols on clean and pre-oxidized Ag(110) surfaces. *Surf. Sci.* **1991**, *257*, 103–112.

(65) Kim, B.; Ma, S.; Molly Jhong, H.-R.; Kenis, P. J. A. Influence of dilute feed and pH

on electrochemical reduction of CO_2 to CO on Ag in a continuous flow electrolyzer. *Electrochim. Acta* **2015**, *166*, 271–276.

(66) Yang, H.; He, L. Q.; Hu, Y. W.; Lu, X.; Li, G. R.; Liu, B.; Ren, B.; Tong, Y.; Fang, P. P. Quantitative detection of photothermal and photoelectrocatalytic effects induced by SPR from Au@Pt nanoparticles. *Angew. Chem. Int. Ed. Engl.* **2015**, *54*, 11462–11466.

Graphical TOC Entry

Plasmon-induced CO desorption enhances CO/H₂ selectivity